Oxidation of CO over gold supported on Zn-modified Ceria catalysts

O.H. Laguna*, M.A. Centeno, F. Romero-Sarria, J.A. Odriozola

Departamento de Química Inorgánica e Instituto de Ciencia de Materiales de Sevilla, Centro Mixto Universidad de Sevilla-CSIC, Avenida Américo Vespucio 49, 41092 Seville, Spain

*Corresponding author: oscarh@icmse.csic.es Tel: +34 954489221 / FAX: +34 954460665

Abstract

A series of Zn-modified ceria solids were prepared by thermal decomposition of the corresponding metal propionates. The formation of segregated ZnO particles on the ceria surface is evidenced for these solids using X-ray diffraction; in addition to this the characterization data may allow discarding the formation of a $ZnO\text{-}CeO_2$ solid solution. On modifying with Zn, the reducibility of the ceria support is enhanced, being the highest reducibility the one obtained for the $ZnO\text{-}CeO_2$ solid having a 1:9 Zn:Ce atomic ratio (CeZn10). The activity of this solid in the CO oxidation reaction was the highest among the tested Zn-modified ceria solids. Therefore, catalysts containing 1 wt.% gold, supported on pure ceria and CeZn solids, were prepared, characterized and their catalytic activities tested. The Zn-modified gold catalyst is more active than the un-modified Au/CeO_2 catalyst in the oxidation of CO; this behavior is related to the higher metallic dispersion of gold on the CeZn support surface. However, the number of oxygen vacancies acting as nucleation sites for gold, is hardly modified in the Zn-modified ceria support and, therefore, the higher gold dispersion must be related to high electron density sites on the catalyst surface as a result of Au-Ce-Zn interaction, this improved gold dispersion results in higher activities for CO oxidation.

Keywords

1) Gold catalysts 2) Zn-modified Ceria 3) CO oxidation 4) Oxygen vacancies

1. Introduction

CO abatement reactions, as CO oxidation [1], water gas shift (WGS) [2] or preferential CO oxidation (PROX) [3] play a key role from environmental and technological points of view. In particular, CO oxidation from H_2-rich reformate gases is crucial when hydrogen is used in polymer electrolyte fuel cells [4].

The high catalytic activity of gold catalysts in the CO oxidation reaction at low temperatures has been widely demonstrated [5, 6]. This high activity is frequently associated to the gold particle size [7]. High metallic dispersion for gold-supported materials (with gold particles sizes typically below 5 nm), it is achieved through the enhancement of the metal-support interaction [8].

The existence of structural defects in the support surface, e.g. oxygen vacancies, plays a determinant role in gold metallic dispersion leading to smaller gold particles which in turn results in an enhanced activity in CO oxidation [1, 9, 10]. Therefore, CeO_2-based materials are very attractive support for gold catalysts, as a result of their oxygen exchange capability which is closely related to the occurrence and diffusion of oxygen vacancies in the structure. These point defects can act as nucleation sites for gold deposition [10, 11]. The use of aliovalent cations, such us Cu [12, 13], Zr [14, 15], Fe [16, 17] or Eu [18],for modifying the CeO_2 structure is a widely studied alternative to improve the oxygen exchange ability of CeO_2. On modifying ceria solids with Zn the reducibility and oxygen exchange abilities of CeO_2 is enhanced [19, 20]. However, the Ce-Zn interaction mechanism is under discussion, both the formation of a Zn-Ce solid solution [20] and segregation of the oxides [19], has been proposed as responsible for the Ce-Zn synergy.

It has been previously reported that gold nucleates on oxygen vacancies at the ceria surface and forms 3D clusters growing epitaxialy on the (0001) plane of ZnO [11]. On the other hand, an excellent matching is found between the Zn and Ce atomic positions for the CeO_2 and ZnO planes perpendicular to the (111) and (0002) directions of the CeO_2 and ZnO solids, respectively [21, 22]. This epitaxial growth has been proposed to result in oxygen vacancies in ZnO that are also the active sites in methanol synthesis over Au/ZnO, and that the presence of the Au particles enhances the number of exposed oxygen vacancies in ZnO, presumably located at the interface region [22].

Considering this scenario, we study in this work a series of gold catalysts prepared with Zn-modified ceria supports having variable amounts of the modifying agent, this way the Ce-Zn synergy might be evaluated in supported gold catalysts using the CO oxidation reaction as a test.

2. Materials and methods

2.1. Synthesis of the catalysts: A series of Ce-Zn mixed oxides (Zn content of 10, 25 and 50 mol%) were synthesized by a pseudo sol-gel method involving the thermal decomposition of the corresponding propionates. These propionates were produced after dissolution of the adequate amounts of Ce(III) acetate and Zn(II) acetyl acetonate in propionic acid (0.12 M). The propionic acid excess was retired from the mixture through simple distillation obtaining a resin-like that is further calcined at 500 ºC for 2h in air. For the sake of comparison an un-modified ceria sample was synthesized by the same procedure [23]. Samples were identified as CeZnX where X accounts for the Zn molar percentage.

Gold catalyst (1 wt.%) were prepared by the deposition-precipitation method over selected supports (CeZn10 and CeO_2), at 70ºC and pH=8 using chloroauric acid as gold source. The

obtained solids (Au/CeZe10 and Au/CeO_2) were washed with deionized water until total chloride removal, dried overnight at 60°C and finally, calcined for 2h at 300 ºC.

2.2. Characterization: X-ray fluorescence (XRF) spectrometry was carried out in an X Panalytical® AXIOS PW4400 instrument equipped with an Rh tube. The measurements were taken onto pressed pellets containing 6 wt.% of wax. Powder X-ray diffraction (XRD) patterns were recorded on a Siemens® D500 spectrometer, using Cu Kα radiation, 0.05° step size and 1 s step time. Textural properties were studied by N_2 adsorption/desorption isotherms at liquid nitrogen temperature using a Micromeritics® ASAP 2010 apparatus. Before analysis, the samples were degassed at 150 ºC for 2 h in vacuum. Raman spectra were recorded in a dispersive Horiva Jobin Yvon LabRam HR800 Confocal Raman Microscope with a 20-mW green laser (532.14 nm) without filter and using a 600 grooves/mm grating. The microscope used an objective with a confocal pinhole of 100 μm.

A homemade apparatus with a conventional quartz reactor connected to a TCD was used for obtaining the TPR profiles. In every experiment, 50 mg of sample was placed in the reactor and submitted to a 5% H_2/Ar gas flow (50 mL/min). Then, a heating rate of 10 ºC/min to a final temperature of 900 ºC was set. The H_2 consumption was monitored and compared with a CuO pattern.

A Zeiss ULTRA 55 high-resolution FESEM microscope equipped with in lens, secondary and backscattered detectors, was used for analyzing the gold particle size distribution.

2.3. Catalytic activity: For the CO oxidation reaction, the catalysts were pretreated for 1 h at 300ºC in a 30 mL/min activation flow of 21% O_2 balanced in He. The light-off curves (from room temperature to 300 ºC, 5ºC/min) were obtained with a 42 mL/min reactive stream of 3.4% CO and 21% O_2 in He. The reaction was carried out in a conventional continuous flow U-shaped glass reactor working at atmospheric pressure where 80 mg of sample were placed

between glass wools. The reaction was followed by mass spectrometry (Balzers® Thermostar).

3. Results and discussion

3.1. Ce-Zn mixed oxides: The chemical composition of the prepared solids is quite close to the targeted ones 10%, 25% and 50% (table 1), which is in accordance with our recent reports where we demonstrated the successful synthesis of M-modified CeO_2 systems (M=Zr, Zn, Fe) by the same methodology [17, 24]. BET surface area values of the Zn-modified systems do not present important modifications with regard to the bare CeO_2 (table 1).

Figure 1 presents the XRD patterns of the prepared solids are presented in figure 1. In all cases reflections corresponding to the c-CeO_2 fluorite structure (JCPDS 00-034-0394) are observed. Besides this, additional reflections corresponding to the existence of ZnO with hexagonal structure (zincite) are observed for the Zn-modified solids (JCPDS 36-1451) [15, 25]. The addition of Zn does not modify the c-CeO_2 lattice parameter discarding the formation of a Ce-Zn solid solution while the presence of diffraction lines corresponding to the ZnO indicates segregation of this phase even in the case of the solid with the lowest Zn content studied. Assuming complete immiscibility of CeO_2 and ZnO phases and an epitaxial growth of the ZnO phase on the ceria surface previously reported [21, 26], a Zn surface coverage of ca. 8 Zn atoms per square nanometer would be estimated in the case of the CeZn10 solid. This Zn surface coverage would be slightly higher than the number of surface oxygen sites present on the ceria surface, therefore accounting for very small diffraction lines observed for this solid (insert in figure 1).

On the other hand, the higher the Zn contents of the support, the lower the ceria crystallite size, estimated using the Scherrer equation (figure 2). This behavior has been previously

reported for modified CeO_2 and evidences that ZnO hinders mass transportation during calcination and restricts grain growth substantially [15, 17, 27, 28].

The Raman spectra of the prepared solids are shown in figure 2. The spectra of all solids are similar and characterized by the signals corresponding to the symmetric breathing mode (F_{2g}) of oxygen atoms around Ce^{4+} ions [15, 29, 30] at 460 cm^{-1} and a fairly low intensity band at ca. 600 cm^{-1} (figure 2 insert) commonly attributed to the presence of oxygen vacancies (Ov) [15, 29, 30]. The evaluation of the area of the oxygen vacancies (Ov) signal to the F_{2g} signal ratio has been previously reported as the most appropriate way of comparing the population of oxygen vacancies in different solids [16, 29]. The Ov/F_{2g} area ratio values obtained for the studied supports (figure 3) show that the addition of Zn does not generate additional oxygen vacancies in the CeO_2 oxide for the solids with 25 and 50 Zn mol.%. This Ov/F_{2g} ratio even slightly decreases. The observed decrease of the Ov/F_{2g} Raman signal ratio for the CeZn25 and CeZn50 solids can be related with the formation of ZnO islands, clearly evidenced by XRD (figure 1). The ZnO islands are therefore blocking surface oxygen vacancies of the CeO_2 structure, which is in accordance with ceria particle size growth inhibition by ZnO islands [15, 17, 27, 28].

The TPR profiles of the studied supports are presented in figure 4. Pure CeO_2 presents two main reduction signals. Surface reduction of Ce^{4+} species resulted in the peak at 522 ºC, the second one at higher temperature (781 ºC) corresponds to the bulk reduction of CeO_2 [31]. Naknam et al. [32] did not observe intrinsic reducibility of pure ZnO in Au/Zn and Au/ZnO-Fe_2O_3 catalysts tested for the preferential oxidation of CO (PROX). They established that none of the observed reduction process could be associated to ZnO. On modifying with ZnO the low temperature reduction peak shifts towards lower temperatures appearing in the presence of ZnO at 390 ± 10 ºC, whereas the high temperature reduction peak shifts monotonically to higher temperatures on increasing the ZnO content, showing a maximum at

888 ºC for the catalyst with the highest ZnO loading. Our results clearly state that on modifying with ZnO the catalyst reducibility is enhanced as early reported [20, 33]. Several factors may be invoked for explaining these results: synergy between oxides as a result of the intimate contact between both oxides CeO_2 and ZnO allowing the enhancement of the surface reducibility of the Ce^{4+} species, the reduction of Zn^{2+} species and/or a strong modification of the surface-to-volume ratio of the ceria particles upon ZnO addition. The formation of oxygen vacancies in ZnO, in the presence of a 5% H_2-95% Ar stream, is thermodynamically favored being observed at temperature above 450 ºC [34]. On the other hand, if the thermodynamics of the formation of cerium oxides [35, 36] is also taken into account, the formation of oxygen vacancies in ZnO, V_o^x, when in close contact with ceria may react with cerium oxide as follows, where O_o^x is a lattice oxygen in ZnO:

$$2CeO_2 + V_o^x \leftrightarrow Ce_2O_3 + O_o^x \qquad \text{(Eq. 1)}$$

According to the thermodynamic shown in [34-36], the free energy for Eq. 1 is given by $\Delta G = -54310 + 8T$ (J/mol), where ΔG is the free Gibbs energy and T is temperature. Therefore the formation of oxygen vacancies in the ZnO phase favors the reducibility of the ceria phase. This mechanism, formation of an oxygen vacancy in the ZnO phase that is further oxidized by the reduced ceria phase, accounts for the synergy between both phases and for a certain reduction of the ZnO phase. Beside this, the crystallite size of the ceria phase reduces upon ZnO addition. As mentioned above, this must be related to the pinning of the particle growth mechanism by the presence of ZnO resulting in nanometric powders. If we assume, for the sake of simplicity, spherical morphology for the ceria particles, the particle size decrease from ca. 14 to ca. 10 nm upon addition of ZnO results in a surface-to-volume ratio 1,5 times higher for the samples containing the highest amount of ZnO than for the pure ceria phase. This

change in the surface-to-volume ratio may also favor the low temperature reducibility shifting the surface reduction peak to lower temperatures.

The high-temperature signal shift to higher temperatures on increasing the Zn amount is more complex because ZnO loss due to evaporation may increase rapidly at temperatures over 700 ºC, up to 60 % weight loss may be expected when heating bulk ZnO at 900 ºC partially by ZnO loss through evaporation and partially by oxygen vacancy formation [34]. By measuring hydrogen consumption through the area under the reduction curves (low and high-temperature peaks) a reducibility increase for the CeZn10 solid with respect to pure CeO_2 is observed, but progressively the reducibility decreases as the amount of Zn is augmented. To have a quantitative estimate for the reducibility of the studied samples, the reduction percentage (RP) of every system has been calculated according to Eq. (2).

$$RP = \frac{E_{HC}}{T_{HC}} \times 100 \qquad \text{Eq. (2)}$$

Where, T_{HC} is the theoretical hydrogen consumption (in moles) required for the complete reduction of all reducible cations in the solid and E_{HC} is the experimental total hydrogen consumption measured during the TPR. For the calculation of T_{HC} we have considered that Ce and Zn are initially in their maximum oxidation state. The obtained results are presented in figure 5.

The solid modified with 10 mol% Zn has a slightly higher reduction percentage than pure CeO_2. This necessarily determines that either the reducibility of cerium oxide is enhanced or zinc reduction occurs, the occurrence of both processes cannot be, however, ruled out as discussed above. On increasing the Zn loadings a lower reduction percentage is observed. From these results, it can be inferred that surface reducibility of the CeZn10 solid is enhanced with respect to the pure oxides. If we consider that ZnO particles are not reducible, CeO_2

reducibility would increase up to reduction percentage of 75%; on the contrary, if we consider that CeO_2 reducibility remains unaltered ca. 90% reduction of the ZnO phase must be considered if ZnO evaporation is not taken into account. The structural data, together with the TPR data, suggest the formation of a monolayer of ZnO growing epitaxialy on the CeO_2 (111) surface. Simply geometrical calculations allows calculate ca. $4x10^{20}$ oxygen sites on the (111) surface of the synthesized ceria nanoparticles and for the CeZn10 solid a number of $4.4x10^{20}$ Zn cations; the incipient ZnO diffraction peak (figure 1) observed for the CeZn10 solid let us assume, for this sample, the epitaxial growth previously reported [21, 26]. This monolayer formation having metal-oxygen distances slightly distorted enhances the solid reducibility. At higher ZnO loadings, ZnO islands start to grow on top of the distorted ZnO monolayer being bigger the size of the islands; these becoming a physical barrier for the reduction of CeO_2. This is in agreement with the data reported by Larese et al. in their study of the oxygen storage and release properties of CeO_2 and Ce-Zr-O systems modified with phosphorus [37]. The formed $CePO_4$ species are located at the surface/subsurface layer of the mixed materials and reduce the specific rate of the oxygen diffusion in the surface and the bulk, decreasing consequently the reducibility.

The catalytic activity in the oxidation of CO of the studied supports is presented in figure 6. Pure ceria shows a poor catalytic activity converting ca. 10% CO to CO_2 at 300ºC. The modified solids (CeZn10 and CeZn25) present higher activities in the CO oxidation reaction than the parent CeO_2 support but on increasing the amount of ZnO loaded to 50% molar the catalytic activity for the oxidation of CO decreases to values similar to the un-modified material. This result must be related with the inhibition observed in the reducibility of this sample due to the bigger size of the ZnO particles.

From all above, considering that the CeZn10 is the support with the highest reducibility (figure 5), and that one that presents the higher efficiency of CO_2 yield as a function of the incorporated Zn (figure 6), this solid was selected as support for preparing a gold catalyst (Au/CeZn10) that will be compared with a non-modified Au/CeO_2 one.

3.2. Gold catalysts: The gold content of the catalysts (1 wt.%) approaches quite well the target values (1 wt.%). Upon gold deposition, the BET surface area of the Au/CeZn10 catalysts slightly increases with respect to that of the corresponding support (table 1). This common phenomenon in gold catalysts is usually explained assuming that the gold nanoparticles inside the ceria pores enlarges the pore size and generates a higher surface area [38, 39]. XRD patterns (not shown) are similar to those of the supports without additional reflections associated to the presence of gold. This suggests a small size for gold nanoparticles deposited on the support surface.

On the other hand, the band associated to oxygen vacancies is absent in the Raman spectra of the prepared gold catalysts (figure 7). Therefore, oxygen vacancies, as demonstrated for other systems [15, 18, 40, 41], act as preferential structural positions for the nucleation of gold nanoparticles on CeO_2 and CeZn10 oxides. The number of surface oxygen vacancies is higher in the Zn-modified support as stated above, accordingly, FESEM micrographs of the gold catalysts (figure 8) show that the number of gold nanoparticles with diameters between 4 and 19 nm is smaller for the Au/CeZn10 catalyst. Considering that gold nanoparticles with diameters below 4 nm are indistinguishable using FESEM and that both catalysts have the same noble metal loading (table 1) the FESEM results support the smaller average gold particle size of the Au/CeZn10 catalysts. The higher gold dispersion in Au/CeZn10 probably means that gold deposition takes place mainly at the surface interface sites where the Ce-Zn

interaction is stronger; these sites should have the highest electron density as a result of the slight mismatch between the CeO_2 and ZnO surfaces [15].

In the TPR profiles of the gold catalysts the high temperature peak remains unaltered with respect to the TPR profile of the parent support (figure 9). Therefore, the bulk reducibility of the supports is hardly affected by the presence of gold, being mainly dominated for the balance between the energy of the oxygen vacancy formation and the free energy of formation of water. However, the low temperature reduction peak shifts to even lower temperatures upon gold addition. In this case of the pure ceria support this peak has a maximum at 197 ºC whereas for the Zn-modified support there is not a well-defined peak but a broad almost featureless profile extending from ca. 125 to 600 ºC. Although, some authors have argued that the low temperature peak in the TPR profile of Au/ZnO catalyst were associated to the reduction of Au^{3+} within the internal of 150-200 ºC [32], we must rule out this possibility since these low temperature reduction processes account, in the case of gold catalysts for 54± 1% of the total reducible species. However, the presence of some Au^{+} [42] or even Au^{3+} [43] species cannot be fully discarded. The different shapes of the TPR profile traces for pure and Zn-modified catalysts should be associated to differences in the coordination environments of surface Ce^{4+} species that may have a next nearest neighbors either cerium or zinc cations in different positions. Hydrogen spillover from gold nanoparticles may influences the mechanism proposed in eq. 1, resulting in more complex synergies between gold, zinc oxide and ceria. Although, it is difficult to separate the reduction of every cation as an independent process, the synergy between the three components of the catalyst is promoting the reducibility since the low temperature reduction process shows a peak at 154 ºC.

Stoichiometric CeO_2 has a cubic fluorite structure with a lattice constant of 0.541 nm usually exposing the (111) plane [44], pure ZnO having the hexagonal wurzite structure preferentially expose the (0002) plane. The two planes have the same 2D symmetry but a slight mismatch in

the lattice constant of 0.040 nm; as a result, the Ce-O-Zn bonds deviate from the equilibrium distance for the pure solids enhancing the solid reducibility. The presence of gold on the CeZn10 support further modifies the energetic of the surface particularly upon reduction since the surface energy of the ceria surface induces surface reconstruction as a function of the number of surface defects [36]. All these processes may promote electronic exchanges increasing surface oxygen reactivity allowing an easy oxygen exchange in the Au/CeZn10 catalyst.

The catalytic activity of the gold catalysts is presented in figure 6. Both samples present much better catalytic performances than the corresponding support, reaching 100% CO conversion at temperatures below 150ºC, and being Au/CeZn10 catalyst more active than Au/CeO_2. This better catalytic activity agrees with the lower gold particle size and higher dispersion of gold nanoparticles observed by FESEM for the Au/CeZn10 system. In addition, the improvement in the CO conversion could be explained by the enhancement of the surface reducibility in this sample (figure 9). The Au-Ce-Zn interaction promotes the reducibility of the system and consequently, its oxygen exchange ability, required for the CO oxidation reaction.

4. Conclusions

A series of Zn-modified ceria solids were prepared by thermal decomposition of the corresponding metal propionates. The formation of segregated ZnO islands on the ceria surface is evidenced for these solids using X-ray diffraction; in addition to this, the characterization data allow discarding the formation of a CeO_2-Zn solid solution.

On modifying with Zn, the reducibility of the ceria support is enhanced, being the highest reducibility the one obtained for the CeO_2-ZnO solid having a 9:1 Ce:Zn atomic ratio (CeZn10). The activity of this solid in the CO oxidation reaction was the highest among the tested Zn-modified ceria solids. Therefore, catalysts containing 1 wt.% gold, supported on

pure ceria and CeZn10 solids, were prepared, characterized and their catalytic activities tested. The Zn-modified gold catalyst is more active than the un-modified Au/CeO_2 catalyst in the oxidation of CO; this behavior is related to higher metallic dispersion of gold on the CeZn support surface. However, the number of oxygen vacancies acting as nucleation sites for gold, is hardly modified in the Zn-modified ceria support and therefore, the higher gold dispersion must be related to high electron density sites on the catalyst surface as a result of Au-Ce-Zn interaction, this improved gold dispersion results in higher activities for CO oxidation.

5. Acknowledgements

Financial support for this work has been obtained from the Spanish Ministerio de Ciencia e Innovación (ENE2009-14522-C05-01) cofinanced by FEDER funds from the European Union, and from Junta de Andalucía (P09-TEP-5454). O.H. Laguna and F. Romero-Sarria thank the same Ministry for the FPI fellowship (BES-2007-14409) and the Ramón y Cajal contract awarded respectively. Finally, we thank Dr. Juan Almagro (ACERINOX S.A. Spain) for his help with high-resolution FESEM experiments.

6. *References*

[1] F. Romero-Sarria, A. Penkova, L.M. Martinez T, M.A. Centeno, K. Hadjiivanov, J.A. Odriozola, Applied Catalysis B: Environmental 84 (2008) 119-124.

[2] T. Tabakova, V. Idakiev, J. Papavasiliou, G. Avgouropoulos, T. Ioannides, Catalysis Communications 8 (2007) 101-106.

[3] N. Bion, F. Epron, M. Moreno, F. Mariño, D. Duprez, Topics in Catalysis 51 (2008) 76-88.

[4] T.V. Choudhary, D.W. Goodman, Catalysis Today 77 (2002) 65-78.

[5] M. Haruta, N. Yamada, T. Kobayashi, S. Iijima, Journal of Catalysis 115 (1989) 301-309.

[6] J.G. Carriazo, L.M. Martínez, J.A. Odriozola, S. Moreno, R. Molina, M.A. Centeno, Applied Catalysis B: Environmental 72 (2007) 157-165.

[7] M. Haruta, Catalysis Today 36 (1997) 153-166.

[8] M.Á. Centeno, C. Portales, I. Carrizosa, J.A. Odriozola, Catalysis Letters 102 (2005) 289-297.

[9] M.I. Domínguez, F. Romero-Sarria, M.A. Centeno, J.A. Odriozola, Applied Catalysis B: Environmental 87 (2009) 245-251.

[10] F. Romero-Sarria, L.M.T. Martínez, M.A. Centeno, J.A. Odriozola, Journal of Physical Chemistry C 111 (2007) 14469-14475.

[11] S. Chaturvedi, J.A. Rodriguez, Surface Science 401 (1998) 282-295.

[12] D. Gamarra, A. Martínez-Arias, Journal of Catalysis 263 (2009) 189-195.

[13] S. Cruz, O. Sanz, R. Poyato, O.H. Laguna, F.J. Echave, L.C. Almeida, M.A. Centeno, G. Arzamendi, L.M. Gandia, E.F. Souza-Aguiar, M. Montes, J.A. Odriozola, Chemical Engineering Journal (2010) doi:10.1016/j.cej.2010.1008.1088

[14] S. Rossignol, C. Micheaud-Especel, D. Duprez, F.V.M.S.M. Avelino Corma, G.F. José Luis, Studies in Surface Science and Catalysis, Elsevier, 2000, pp. 3327-3332.

[15] O.H. Laguna, F. Romero Sarria, M.A. Centeno, J.A. Odriozola, Journal of Catalysis 276 (2010) 360-370.

[16] H. Bao, X. Chen, J. Fang, Z. Jiang, W. Huang, Catalysis Letters 125 (2008) 160-167.

[17] O.H. Laguna, M.A. Centeno, G. Arzamendi, L.M. Gandía, F. Romero-Sarria, J.A. Odriozola, Catalysis Today 157 (2010) 155-159.

[18] W.Y. Hernández, F. Romero-Sarria, M.A. Centeno, J.A. Odriozola, Journal of Physical Chemistry C 114 (2010) 10857-10865.

[19] J. Papavasiliou, G. Avgouropoulos, T. Ioannides, Applied Catalysis B: Environmental 69 (2007) 226-234.

[20] G. Avgouropoulos, M. Manzoli, F. Boccuzzi, T. Tabakova, J. Papavasiliou, T. Ioannides, V. Idakiev, Journal of Catalysis 256 (2008) 237-247.

[21] J.R. Duclère, B. Doggett, M.O. Henry, E. McGlynn, R.T.R. Kumar, J.P. Mosnier, A. Perrin, M. Guilloux-Viry, Journal of Applied Physics 101 (2007) 013509-013507.

[22] J. Strunk, K. Kähler, X. Xia, M. Comotti, F. Schüth, T. Reinecke, M. Muhler, Applied Catalysis A: General 359 (2009) 121-128.

[23] H. Provendier, C. Petit, J.L. Schmitt, A. Kiennemann, C. Chaumont, Journal of Materials Science 34 (1999) 4121-4127.

[24] F. Romero-Sarria, J.C. Vargas, A.-C. Roger, A. Kiennemann, Catalysis Today 133-135 (2008) 149-153.

[25] E. Moretti, L. Storaro, A. Talon, P. Patrono, F. Pinzari, T. Montanari, G. Ramis, M. Lenarda, Applied Catalysis A: General 344 (2008) 165-174.

[26] A.M. Torres-Huerta, M.A. Domnguez-Crespo, S.B. Brachetti-Sibaja, H. Dorantes-Rosales, M.A. Hernndez-Prez, J.A. Lois-Correa, Journal of Solid State Chemistry 183 (2010) 2205-2217.

[27] Q. Fu, W. Deng, H. Saltsburg, M. Flytzani-Stephanopoulos, Applied Catalysis B: Environmental 56 (2005) 57-68.

[28] T.Y. Ma, Z.Y. Yuan, Q.J.L. Cao, European Journal of Inorganic Chemistry (2010) 716-724.

[29] W.Y. Hernández, M.A. Centeno, F. Romero-Sarria, J.A. Odriozola, Journal of Physical Chemistry C 113 (2009) 5629-5635.

[30] J.E. Spanier, R.D. Robinson, F. Zhang, S.W. Chan, I.P. Herman, Physical Review B - Condensed Matter and Materials Physics 64 (2001) 2454071-2454078.

[31] Q. Fu, A. Weber, M. Flytzani-Stephanopoulos, Catalysis Letters 77 (2001) 87-95.

[32] P. Naknam, A. Luengnaruemitchai, S. Wongkasemjit, Energy & Fuels 23 (2009) 5084-5091.

[33] P. Panagiotopoulou, J. Papavasiliou, G. Avgouropoulos, T. Ioannides, D.I. Kondarides, Chemical Engineering Journal 134 (2007) 16-22.

[34] Y. Kim, S. Kang, Journal of Physical Chemistry B 114 (2010) 7874-7878.

[35] D.J.M. Bevan, J. Kordis, Journal of Inorganic and Nuclear Chemistry 26 (1964) 1509-1523.

[36] M. Fronzi, A. Soon, B. Delley, E. Traversa, C. Stampfl, Journal of Chemical Physics 131 (2009).

[37] C. Larese, M. López Granados, R. Mariscal, J.L.G. Fierro, P.S. Lambrou, A.M. Efstathiou, Applied Catalysis B: Environmental 59 (2005) 13-25.

[38] M.I. Domínguez, M. Sánchez, M.A. Centeno, M. Montes, J.A. Odriozola, Journal of Molecular Catalysis A: Chemical 277 (2007) 145-154.

[39] Z. Kónya, V.F. Puntes, I. Kiricsi, J. Zhu, J.W. Ager, M.K. Ko, H. Frei, P. Alivisatos, G.A. Somorjai, Chemistry of Materials 15 (2003) 1242-1248.

[40] K. Qian, S. Lv, X. Xiao, H. Sun, J. Lu, M. Luo, W. Huang, Journal of Molecular Catalysis A: Chemical 306 (2009) 40-47.

[41] J.J. Plata, A.M. Márquez, J. Fernández Sanz, R. Sánchez Avellaneda, F. Romero-Sarria, M.I. Domínguez, M.A. Centeno, J.A. Odriozola, Topics in Catalysis (2010) Article in press.

[42] Q. Fu, H. Saltsburg, M. Flytzani-Stephanopoulos, Science 301 (2003) 935-938.

[43] C.H. Kim, L.T. Thompson, Journal of Catalysis 230 (2005) 66-74.

[44] A. Pfau, K.D. Schierbaum, Surface Science 321 (1994) 71-80.

TABLE CAPTION

Table 1. Chemical composition and BET surface area of the prepared solids

FIGURE CAPTIONS

Figure 1. XRD pattern of the pure CeO_2 and the Zn-modified solids

Figure 2. Raman spectra of the pure CeO_2 and the Zn-modified solids

Figure 3. Ov/F_{2g} area ratio of the pure CeO_2 and the Zn-modified solids

Figure 4. TPR profile of the pure CeO_2 and the Zn-modified solids

Figure 5. Reduction percentage of the pure CeO_2 and the Zn-modified solids

Figure 6. Catalytic activity during the CO oxidation reaction over the supports and the gold catalysts

Figure 7. Raman spectra of the prepared gold catalysts

Figure 8. SEM micrographs of the prepared gold catalysts

Figure 9. TPR profile of the gold catalysts

Table 1

Solid	Ce (mol.%)♦	Zn (mol.%)♦	Au (wt.%)	BET area (m^2/g)
CeO_2	100	0	--	53
CeZn10	88.3	11.7	--	56
CeZn25	71.8	28.2	--	44
CeZn50	55.0	45.0	--	43
Au/CeO_2	100	0	1.0	54
Au/CeZn10	88.3	11,7	1.1	62

♦ Ce mol.% = 100 x $mol_{Ce}/[mol_{Ce}+mol_{Zn}]$ -- Zn mol.% = 100 x $mol_{Zn}/[mol_{Ce}+mol_{Zn}]$

Figure 1

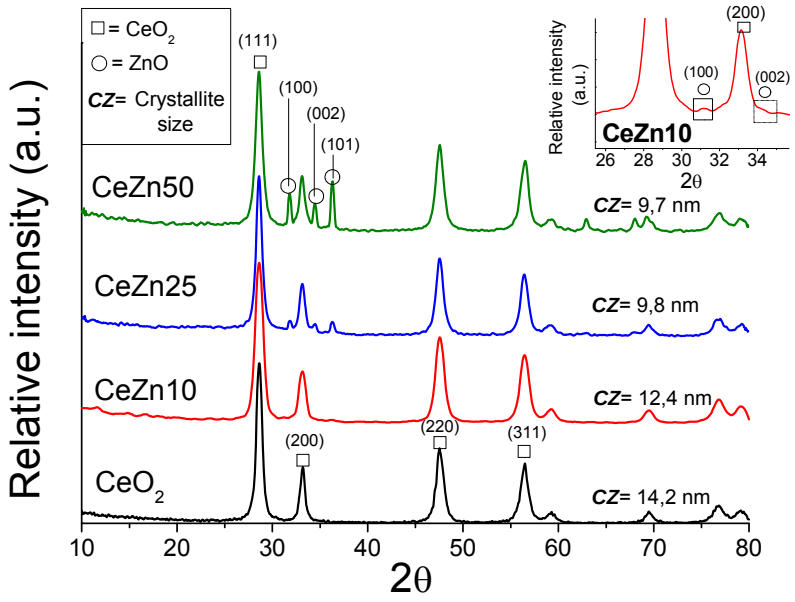
□= CeO2
○= ZnO
CZ= Crystallite size
(111)
(100)
(002)
(101)
CeZn50
CZ= 9,7 nm
CeZn25
CZ= 9,8 nm
CeZn10
CZ= 12,4 nm
(200)
(220)
(311)
CeO2
CZ= 14,2 nm
Relative intensity (a.u.)
2θ
Relative intensity (a.u.)
(200)
(100)
(002)
CeZn10
26 28 30 32 34
2θ

Figure 2

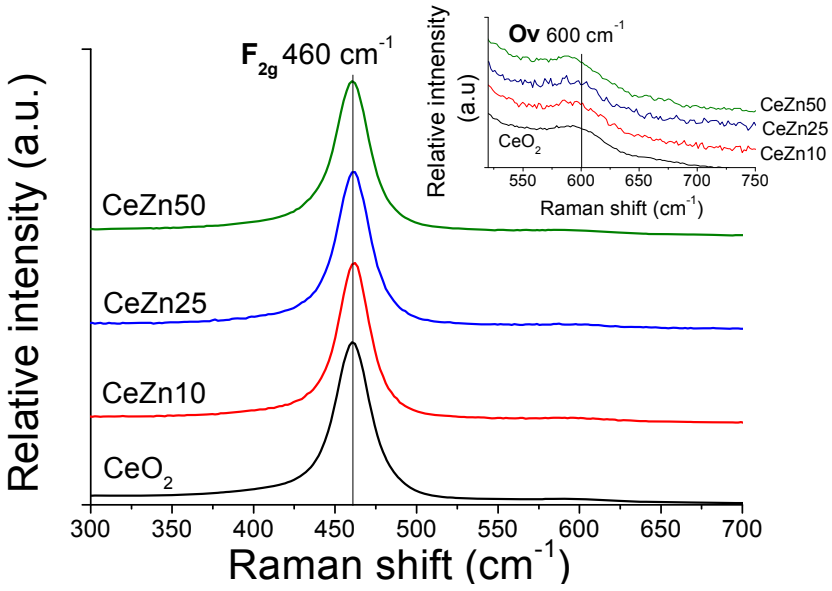
F2g 460 cm-1
Ov 600 cm-1
Relative intnensity (a.u)
CeZn50
CeZn25
CeZn10
CeO2
550 600 650 700 750
Raman shift (cm-1)
Relative intensity (a.u.)
CeZn50
CeZn25
CeZn10
CeO2
300 350 400 450 500 550 600 650 700
Raman shift (cm-1)

Figure 3

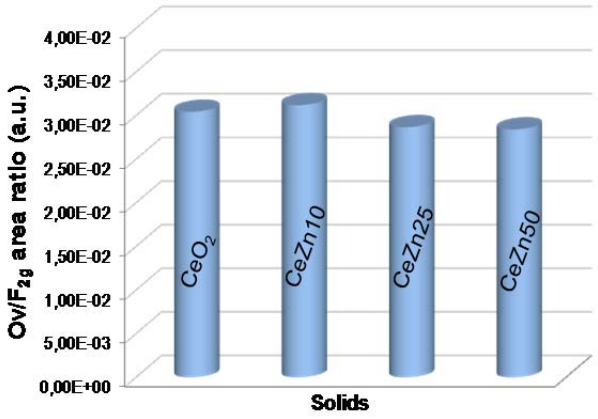
4,00E-02
3,50E-02
3,00E-02
2,50E-02
2,00E-02
1,50E-02
1,00E-02
5,00E-03
0,00E+00
Ov/F2g area ratio (a.u.)
CeO2
CeZn10
CeZn25
CeZn50
Solids

Figure 4

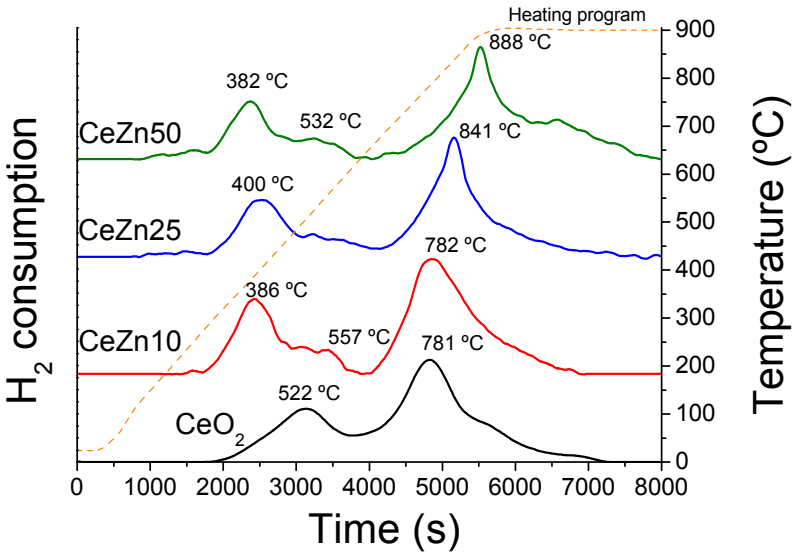
Heating program
888 ºC
382 ºC
532 ºC
841 ºC
CeZn50
400 ºC
CeZn25
782 ºC
386 ºC
557 ºC
781 ºC
CeZn10
522 ºC
CeO2
H2 consumption
Temperature (ºC)
Time (s)
0
1000
2000
3000
4000
5000
6000
7000
8000
0
100
200
300
400
500
600
700
800
900

Figure 5

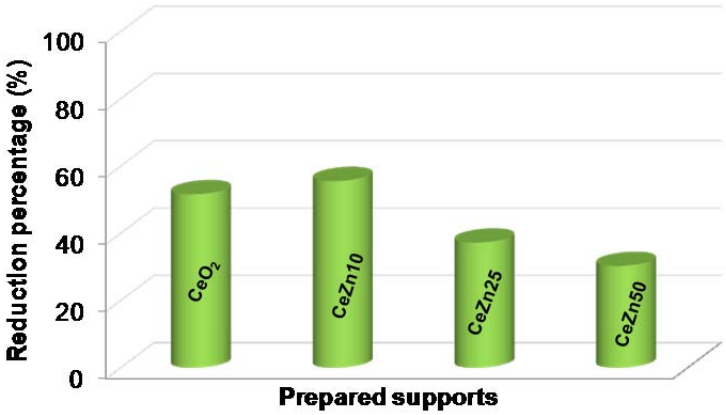
Reduction percentage (%)
100
80
60
40
20
0
CeO2
CeZn10
CeZn25
CeZn50
Prepared supports

Figure 6

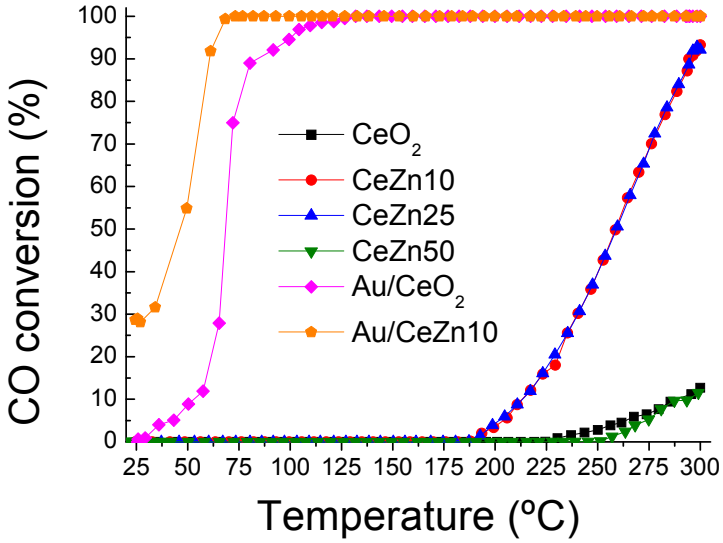
CO conversion (%)
Temperature (ºC)
CeO2
CeZn10
CeZn25
CeZn50
Au/CeO2
Au/CeZn10
0
10
20
30
40
50
60
70
80
90
100
25
50
75
100
125
150
175
200
225
250
275
300

Figure 7

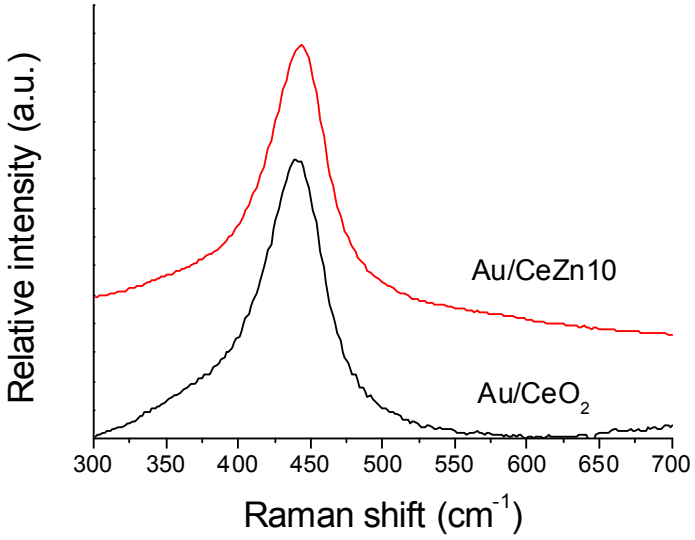
Relative intensity (a.u.)
Au/CeZn10
Au/CeO2
300
350
400
450
500
550
600
650
700
Raman shift (cm-1)

Figure 8

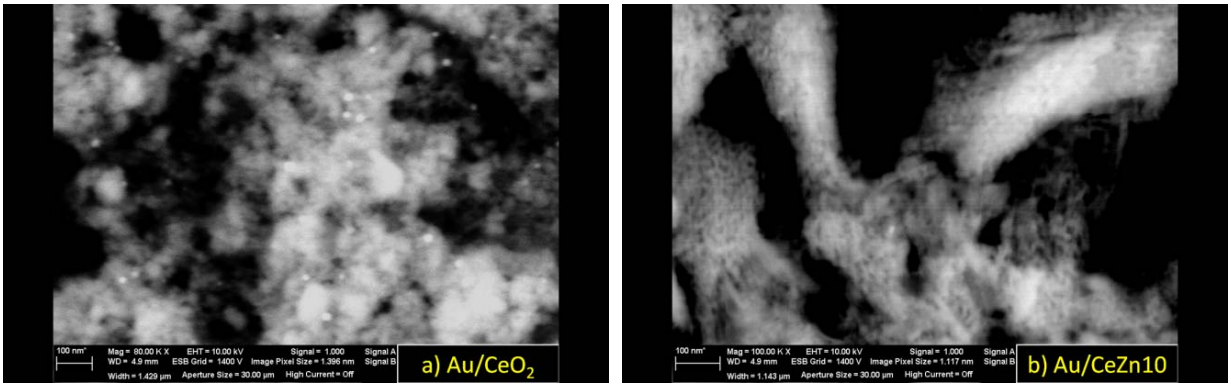

Figure 9

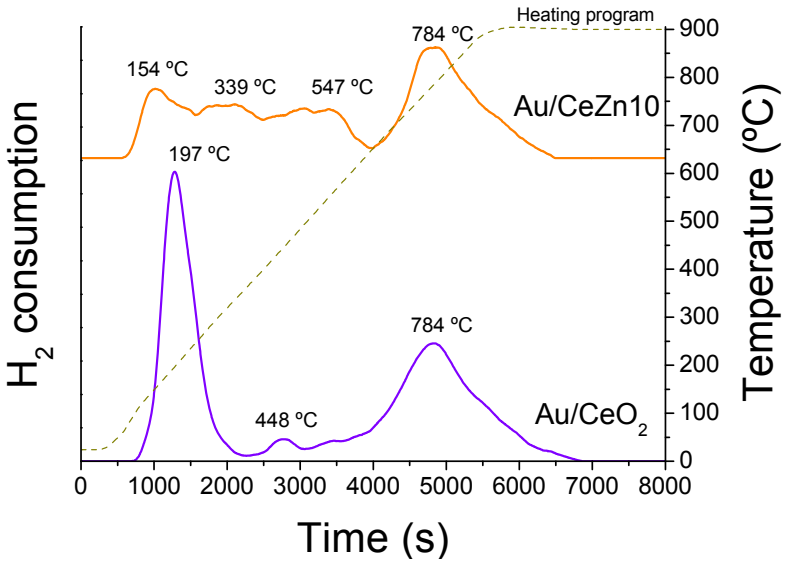
Heating program
784 °C
154 °C
339 °C
547 °C
Au/CeZn10
197 °C
784 °C
448 °C
Au/CeO2
H2 consumption
Temperature (°C)
Time (s)
0
1000
2000
3000
4000
5000
6000
7000
8000
0
100
200
300
400
500
600
700
800
900